




Simplified level set discrete element modeling of particle suspension flows in microfluidics: clogging statistics controlled by particle friction and shape

Ziran Zhou¹ · Rigoberto Moncada¹ · Nathan Jones¹ · Jacinto Ulloa¹ · Xiaojing Fu¹ · José E. Andrade¹ 

Received: 7 August 2023 / Accepted: 29 January 2024 / Published online: 9 March 2024
© The Author(s), under exclusive licence to Springer-Verlag GmbH Germany, part of Springer Nature 2024

Abstract

Particulate precipitation, deposition, and accumulation, including the formation of salt and mineral crystals, frequently occur in a wide range of subsurface applications involving multiphase flow through porous media. Consequently, there has been a considerable emphasis on researching and understanding these phenomena. However, modeling particle dynamics in flows through porous media with low Reynolds numbers has always been a challenging problem as it requires resolving fluid flow around the moving solid particles, the solid–solid contact mechanics, and the solid–fluid coupling. The discrete element method coupled with fluid solvers has been widely used to study particle-laden flow. Most fluid–solid numerical schemes involve solving the full or generalized Navier–Stokes equations, which often yields relatively accurate fluid–solid interactions at the cost of computation time and particle shape limitations. In this paper, we present a novel method to study mono-layered particle-laden flow by coupling the level set discrete element method (LS-DEM) with Hele–Shaw flow model. Utilizing the Hele–Shaw flow model allows us to simplify flow computation, while incorporating LS-DEM enables the simulation of arbitrarily shaped particles. Cases of mono-layered particle flow through a simplified micromodel geometry are studied and validated against published experimental results. Moreover, the effects of particle friction and shape on clogging statistics are investigated.

Keywords Particle suspension flow · Discrete element method · Clogging · Particle shape · Microfluidics modeling

1 Introduction

Clogging is a phenomenon that occurs at constrictions, where discrete particles modify pore structures through deposition and create solid barriers that obstruct flow pathways. It is observed in a wide range of natural or engineered systems, including human organs [20], filtration systems [23], colloidal transport [2, 22], and microfluidic devices [29]. Oftentimes, clogging leads to unfavorable behavior such as reduced efficiency and lifetime or even failure of the system [8]. To better understand this phenomenon, efforts have been made to study clogging both experimentally and numerically.

The modeling of particle dynamics during flow through porous media or low Reynolds number environments

imposes notable challenges related to the fluid flow around the moving solid particles, the solid–solid contact mechanics, and the solid–fluid coupling. Passive-tracer-type models describe the particle population as a scalar concentration field [15]. Nonlinear effects such as dispersion or non-Newtonian rheology can be incorporated in this type of model. This method assumes that the particles are Brownian and do not significantly impact the flow regime. Alternatively, stochastic models such as population balance models (PBM) represent the particle population as a statistical distribution [21]. Such a distribution evolves with time and space according to mass conservation laws and the local shear rate of the fluid, leading to particle aggregation or breakup. The aforementioned methods are suitable for describing the collective motions of particles but are limited in describing the solid–fluid coupling that gives rise to highly nonlinear flow dynamics, such as clogging/unclogging regimes [7].

Another common method is particle-resolved modeling, which requires coupling granular mechanics and Stokes flow through a time-evolving fluid domain, shaped by the

✉ José E. Andrade
jandrade@caltech.edu

¹ California Institute of Technology, Pasadena, USA

positions of individual solid particles. The granular mechanics component is often modeled using the discrete element method (DEM) [3]. On the other hand, different schemes for solving interstitial fluid flow, such as computational fluid dynamics (CFD) [14] or the lattice Boltzmann method (LBM) [9], have been used to couple the fluid mechanics component with DEM. These methods are often computationally expensive, limiting their ability to handle large numbers of particles or perform a high number of model realizations required for statistically significant results.

Simplified coupling methods may be considered to address these limitations [25, 30]. A recent example is the dynamic fluid mesh (DFM) coupled DEM method [31], proposed to simulate suffusion in gap-graded soils. This method solves Poisson’s equation for fluid pressure and Darcy’s law for local flow rates, with the simulated solid shapes limited to spheres, as often constrained by the use of traditional DEM.

In this paper, we develop a particle-resolved modeling framework to describe the flow of mono-layered particle suspensions through a fluid-filled Hele-Shaw cell. We assume simplified porous media flow to lower the computational cost, allowing us to explore larger numbers of particles, arbitrary domain sizes, and arbitrary particle shapes in a reasonable computational time. The structure of this paper is as follows: First, we explain the framework of the proposed method. Then, several case studies are explored and compared with recent experiments from Vani et al. [27]. We show reasonable agreement between the simulation results and the experimental data. Finally, we investigate the effects of friction and particle shapes on clogging.

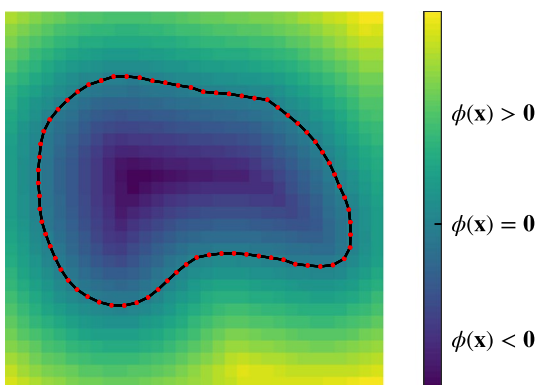
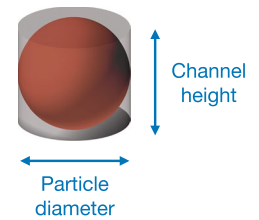


Fig. 1 Level set representation of a 2D arbitrarily shaped particle, with $\phi(\mathbf{x}) = 0$ highlighted by a black contour and surface nodes marked in red (color figure online)

Fig. 2 Illustration of a fluid region occupied by a particle



2 Modeling framework

This section presents the proposed modeling framework, which we divide into three parts: particle–particle contact, particle-fluid coupling, and fluid-particle coupling. The fluid and solid domains are presented in 2D. However, the formulation is extendable to 3D.

2.1 Particle–particle contact

Particle mechanics is modeled using DEM, a numerical method for computing the motion of interacting rigid particles [3]. It has been widely used to simulate the mechanical behaviors of solid aggregates. A recent extension to this method, the level set discrete element method (LS-DEM), has been developed to allow the simulation of arbitrary particle shapes [13] and has been proved accurate in predicting the contact fabrics and dynamics of various 2D and 3D systems [4, 19, 28, 32]. In the LS-DEM framework, the shape of an individual particle is captured by a level set function $\phi(\mathbf{x})$, which calculates the signed distance from an arbitrary point \mathbf{x} to the nearest surface point of the particle. In practice, this function is discretized into a grid (Fig. 1). Each particle is then equipped with a set of nodes uniformly distributed on the surface, where $\phi(\mathbf{x}) = 0$. To check whether a given solid particle is in contact with another, we take the position of each surface point \mathbf{p}_i of the particle in question and perform bilinear interpolation on the other particle’s level set matrix to obtain the level set value $\phi(\mathbf{p}_i)$. A point is inside the other particle (contact exists) if $\phi(\mathbf{p}_i) \leq 0$.

If $\phi(\mathbf{p}_i) < 0$, the contact normal force \mathbf{F}_n and incremental shear force $\Delta\mathbf{F}_s$ are computed as

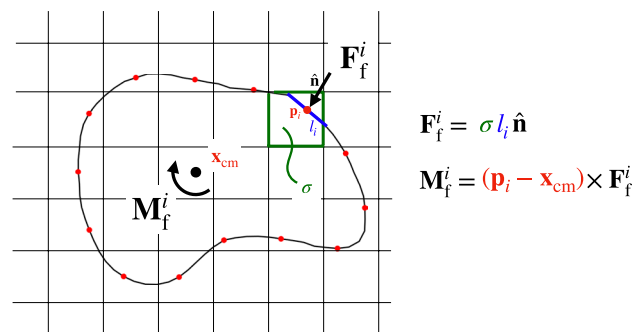


Fig. 3 Illustration of a fraction of fluid force acting on a 2D particle

$$\begin{cases} \mathbf{F}_n = \varphi(\mathbf{p}_i)k_n\hat{\mathbf{n}} - \gamma_n\mathbf{v}_n^{\text{rel}}, \\ \Delta\mathbf{F}_s = k_s\Delta t(\mathbf{v}^{\text{rel}} - \mathbf{v}_n^{\text{rel}}), \end{cases} \quad (1)$$

where k_n and k_s are the normal and shear stiffness of the particles, $\hat{\mathbf{n}}$ is the surface normal at \mathbf{p}_i , γ_n is the normal damping coefficient estimated from the coefficient of restitution C_{res} , \mathbf{v}^{rel} is the relative velocity of the given particle with respect to the contacting particle, and Δt is the integrating time step. The shear force is calculated incrementally in order to accommodate history-dependent behavior with a selected friction law. For instance, employing Coulomb friction with coefficient μ , the shear force is capped as

$$||\mathbf{F}_s|| = \min(\mu||\mathbf{F}_n||, ||\mathbf{F}_s||). \quad (2)$$

The resulting moment due to particle-particle contact is then computed as

$$\mathbf{M} = (\mathbf{p}_i - \mathbf{x}_{\text{cm}}) \times (\mathbf{F}_n + \mathbf{F}_s), \quad (3)$$

where \mathbf{x}_{cm} is the center of mass of the particle. At the end of the particle-particle contact detection, the resultant force and resultant moment are divided by the number of surface nodes in contact to ensure discretization convergence. The reader is referred to Kawamoto et al. [13] for more details on LS-DEM.

2.2 Particle-fluid coupling

For a given particle configuration, to obtain the fluid pressure, a fluid grid that hosts permeability and pressure information is defined, separate from the level set grid of every particle. To solve for fluid pressure, we employ Hele-Shaw flow model and assume an incompressible flow through the pore space between the particles:

$$\nabla \cdot \mathbf{u} = 0, \quad (4)$$

$$\mathbf{u} = -\frac{\kappa(\varphi(\mathbf{x}))}{\eta}\nabla p, \quad (5)$$

where \mathbf{u} is the flux, $\kappa(\varphi(\mathbf{x}))$ is the permeability field that depends on the spatial arrangement of particles, η is the fluid viscosity, and p is the fluid pressure. At each time step, the local permeability and fluid pressure are updated based on the location of every particle. To do this, we loop over the fluid grid cells and check whether the center of each grid cell \mathbf{x} is inside a particle ($\varphi(\mathbf{x}) \leq 0$).

The fluid flow velocity between two parallel plates separated by a distance H can be computed as

$$\mathbf{u} = -\frac{H^2}{12\eta}\nabla p. \quad (6)$$

Combining this expression with Eq. (5), the permeability is calculated within a particle-free region as

$$\kappa(\varphi(\mathbf{x}) > 0) = \frac{H^2}{12}, \quad (7)$$

where H is the gap thickness of the Hele-Shaw cell. Within a solid-occupied region, permeability is estimated by the Kozeny-Carman relation, incorporating a permeability reduction due to the presence of particles. Consequentially, the permeability is updated by

$$\kappa(\varphi(\mathbf{x}) \leq 0) = \Phi_s^2 \frac{\epsilon^3 d^2}{150(1 - \epsilon)^2}, \quad (8)$$

where Φ_s is the sphericity of the particles, d is the average diameter of the particles, and ϵ is the porosity of the grid cells occupied by the particles. Here, the Kozeny-Carman relation makes reference to the system described in Fig. 2. The porosity of the fluid grid cells occupied by the particle is estimated assuming 3D spheres, i.e.,

$$\epsilon = \frac{V_{\text{cylinder}} - V_{\text{sphere}}}{V_{\text{cylinder}}}, \quad (9)$$

where V_{cylinder} is the cross-section of the sphere multiplied by the height of the channel.

To calculate the fluid pressure matrix, we apply finite volume discretization and two-point flux approximation to Eqs. (4) and (5) (see Supplementary Material). In this way, the corresponding second-order PDE can be conveniently simplified and solved as a linear system of algebraic equations with appropriate boundary conditions. Such matrices can be subsequently factorized using a variety of decomposition methods to solve for fluid pressure.

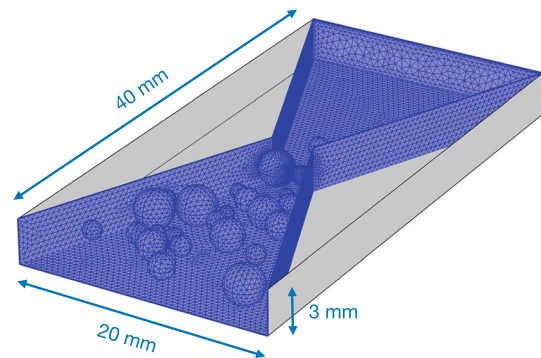


Fig. 4 The finite element mesh of the 3D pore space shaped by particles at the clogged state. The particles are all centered at half of the channel height. The channel height is slightly larger than the diameter of the largest particle. The 3D pressure solution is used to validate the simplifying assumptions of flow in our method

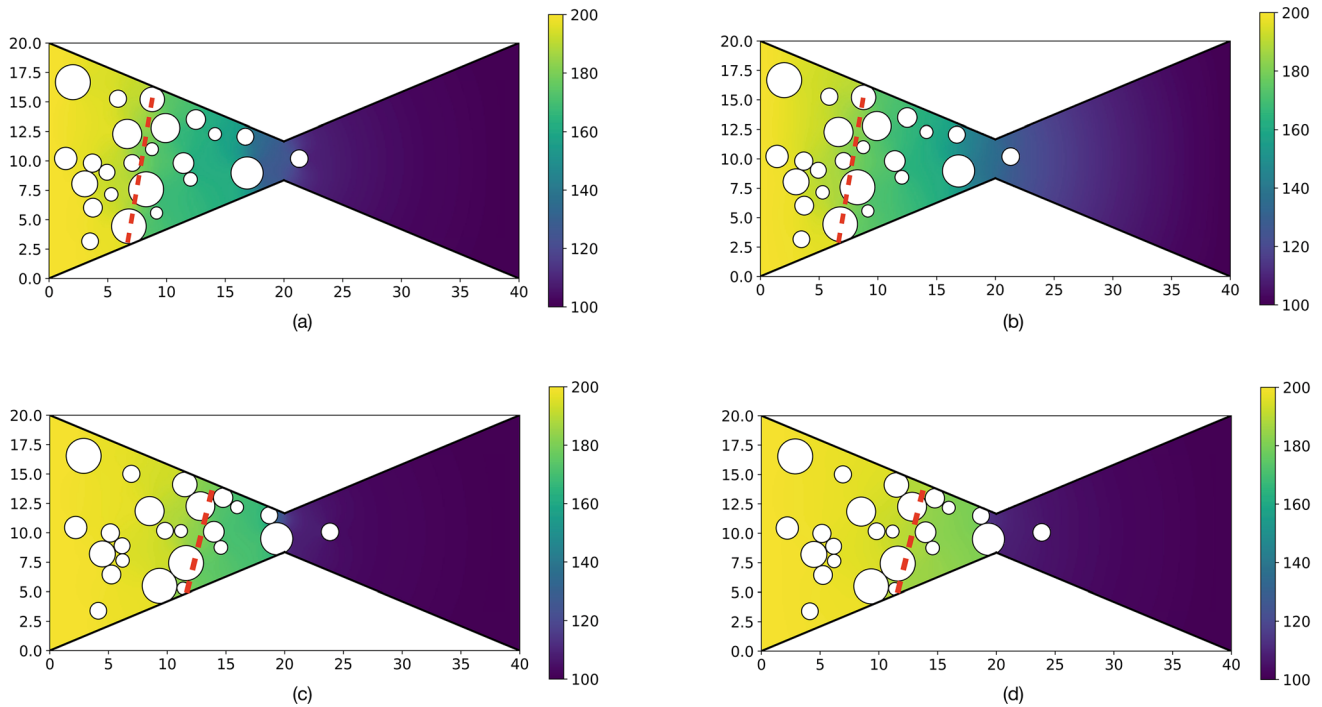


Fig. 5 Left: Gap-averaged pressure field from Stokes equations in 3D within the pore space of the domain at unclogged (a) and clogged (c) states. Right: the corresponding pressure field calculated using the proposed framework at unclogged (b) and clogged (d) states. The color bars show dimensionless pressure. *Note:* in the Stokes flow

solution, the fluid pressure inside the solid region (shown in white color) is nonexistent. In the Hele-Shaw solution, since we assume a reduced permeability in the particle-laden region and a negligibly small permeability outside the hourglass contour, there exists a (masked) finite pressure value inside the solid

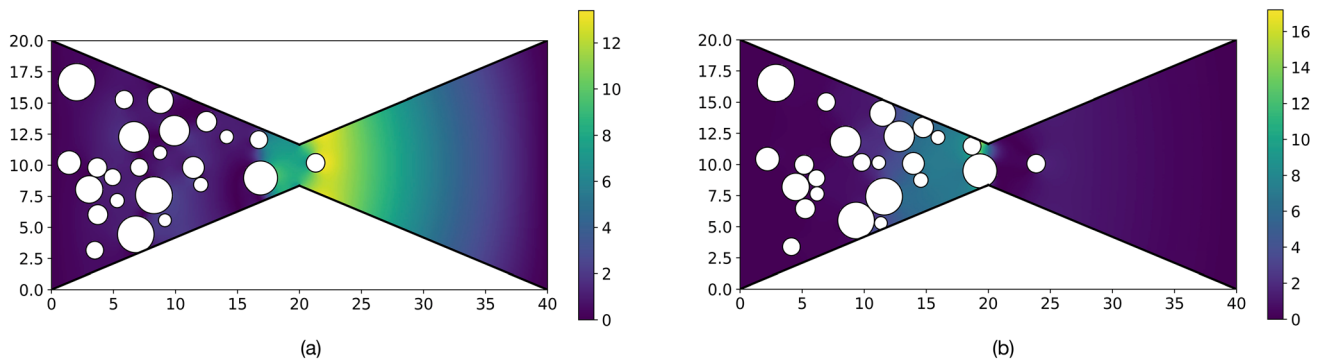


Fig. 6 Relative error of the pressure field (16) computed from the Hele-Shaw flow model and Stokes flow solution at an unclogged state (left) and a clogged state (right)

2.3 Fluid–particle coupling

The level set matrix and discretized surface nodes not only provide a convenient way to track a particle’s surface and the total force exerted through direct particle-particle contact but also offer a computationally efficient method to calculate fluid forces (Fig. 3). In particular, we exert on each surface point of a particle the pressure of the corresponding grid cell where the surface point lies. We then calculate the fraction of fluid force acting on that particular surface point by multiplying the

pressure by a fraction of the particle’s surface area. Thus, the total force \mathbf{F} acting on a particle can be updated by the fluid force as follows:

$$\mathbf{F} = \mathbf{F}_{\text{solid–solid}} + \sum_{i=1}^{N_{\text{nodes}}} \mathbf{F}_f^i \tag{10}$$

Similarly, the total moment \mathbf{M} acting on a particle is updated as

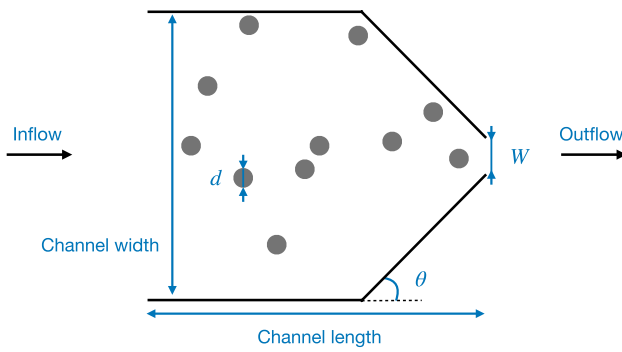


Fig. 7 2D representation of the experimental setup of Vani et al. [27]

$$\mathbf{M} = \mathbf{M}_{\text{solid-solid}} + \sum_{i=1}^{N_{\text{nodes}}} \mathbf{M}_f^i. \quad (11)$$

Here, $\mathbf{F}_{\text{solid-solid}}$ and $\mathbf{M}_{\text{solid-solid}}$ follow from evaluating Eqs. (1)–(3) at each contact and computing the (normalized) resultant force and moment vectors, while \mathbf{F}_f^i and \mathbf{M}_f^i denote the fluid force and moment acting on a surface node \mathbf{p}_i . The fluid force \mathbf{F}_f^i is given by

$$\mathbf{F}_f^i = \sigma l_i \hat{\mathbf{n}}, \quad (12)$$

where σ is the pressure taken from the grid cell where \mathbf{p}_i is located, l_i is the length of the curve around \mathbf{p}_i , and $\hat{\mathbf{n}}$ is the normal at \mathbf{p}_i , perpendicular to the particle surface pointing inward. On the other hand, the fluid moment acting on \mathbf{p}_i is computed as

$$\mathbf{M}_f^i = (\mathbf{p}_i - \mathbf{x}_{\text{cm}}) \times \mathbf{F}_f^i. \quad (13)$$

At each time step, the force (10) and moment (11) are used to update the particle's location and orientation in terms of the corresponding linear acceleration \mathbf{a} and angular acceleration α , computed from Newton's second law:

$$\mathbf{a} = \frac{\mathbf{F}}{m}, \quad (14)$$

$$\alpha = \frac{\mathbf{M}}{I}, \quad (15)$$

where m is the mass of the particle and I is its moment of inertia. The particle's velocity and position can then be determined using explicit time integration methods.

Table 1 Fluid environment properties

| Parameter | Values | Units |
|---|--------|-------------------------|
| Channel height H | 0.95 | (mm) |
| Channel width | 7.8 | (mm) |
| Channel length | 9.2 | (mm) |
| Constriction width to particle diameter ratio $\frac{W}{d}$ | 1.7 | (–) |
| Constriction angle θ | 45 | (deg) |
| Dynamic viscosity η | 75 | (mPa) |
| Inflow rate Q (left boundary condition) | 1 | (mL.min ⁻¹) |
| Outlet pressure (right boundary condition) | 1 | (atm) |

3 Validation

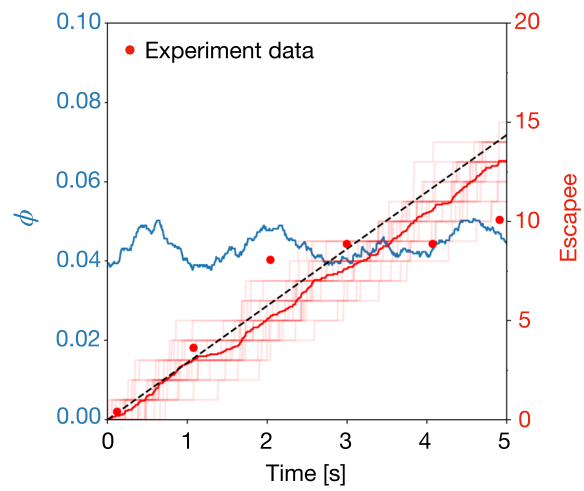
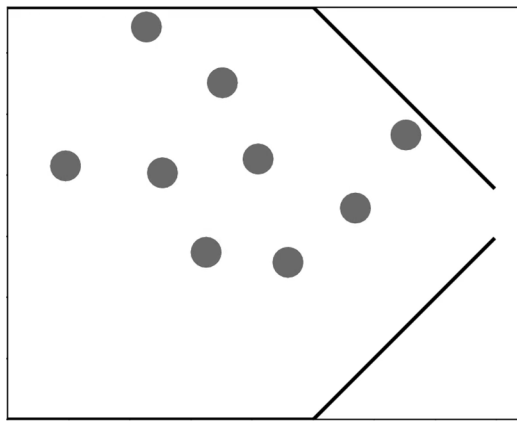
The proposed framework is validated in two parts. In the first subsection, we compare the pressure field computed using the Hele-Shaw flow model with the results obtained from Stokes flow at specific time instances. This validation ensures the consistency and accuracy of the pressure field calculations. In the second subsection, we compare the particle statistics over time with experimental results from Vani et al. [27].

3.1 Comparison of pressure distribution against 3D Stokes flow solution

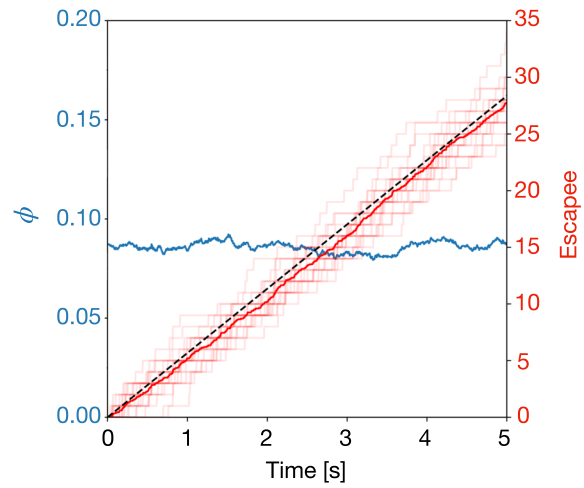
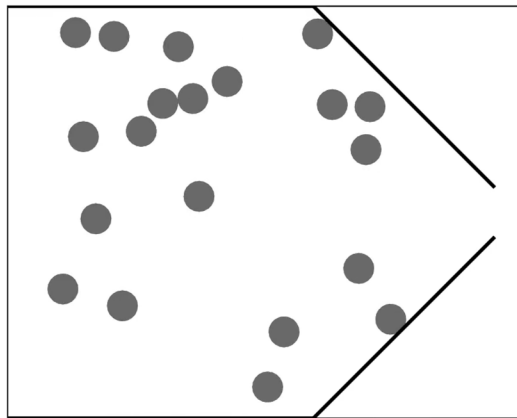
To validate the pressure field produced by our modeling framework, we release a group of 24 particles of different sizes from left to right through an hourglass-shaped constriction using 2D DEM, until a clog forms. In this study, we use dimensionless units for fluid with unit density and viscosity. We assume that the particles and the fluid have the same density, and that the particle centers align with the center of the Hele-Shaw gap. The prescribed dimensionless pressure is 200 at the left boundary and 100 at the right boundary. The region outside the hourglass contour is assumed to have negligibly small permeability. Since all particles are perfect circles, the sphericity Φ_s in Eq. (8) is 1.

Table 2 Particle properties

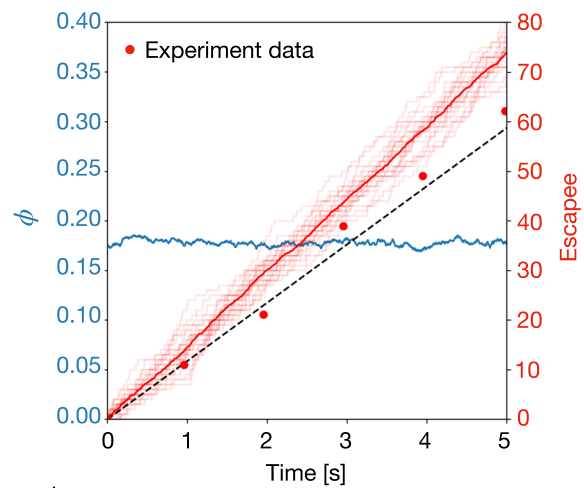
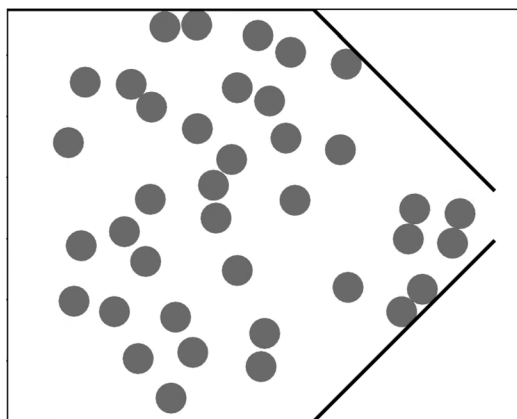
| Parameter | Values | Units |
|---|--------|-----------------------|
| Diameter d | 581 | (μm) |
| Density ρ | 1.049 | (g.cm ⁻³) |
| Young's Modulus E | 3250 | [MPa] |
| Poisson's ratio ν | 0.325 | (–) |
| Friction μ | 0.25 | (–) |
| Coefficient of restitution C_{res} | 0.55 | (–) |
| Global damping ξ | 420 | (s ⁻¹) |



(a) Average $\phi = 0.043$



(b) Average $\phi = 0.086$



(c) Average $\phi = 0.18$

Fig. 8 Left: snapshots of simulations at different packing fractions ϕ . Right: instantaneous packing fraction ϕ (blue) and time-evolution of the cumulative number of escapees from our simulations (red curves), the reference experiments (red dot), and the empirical relation (17) (dashed black curve). The packing fraction is averaged over 20 simulations. The time-evolution of cumulative number of escapees of all 20 simulations are shown in light red curves, and the averaged escapee value is shown in solid red curve. Experimental values from Vani et al. [27] are taken for comparison in (a) and (c). Note that in (a), experimental escapee values fluctuate significantly due to the small prescribed packing fraction; this fluctuation is less obvious in the simulation results due to the averaging process (color figure online)

We then extract the 2D pore geometry at two fixed time instances, one at an unclogged state and the other at a clogged state, and solve the Stokes flow equations through the reconstructed 3D pore space using the finite element method (FEM) implemented in COMSOL. We impose the same inlet and outlet pressure condition and no-slip condition at both the hourglass contour and the particle surfaces. Figure 4 shows the 3D mesh for a clogged state used in the FEM calculation.

We employ the gap-averaged pressure from the full 3D Stokes flow solution (Fig. 5a, c) as a benchmark for the 2D pressure field produced by the proposed Hele-Shaw flow model (Fig. 5b, d). We choose a grid resolution that is sufficiently high to guarantee convergence in the fluid pressure.

In general, we observe some mismatch in pressure magnitude but find an overall good agreement in the spatial distribution of pressure around the particle-occupied region. The yellow-to-green transition region in the pressure field, as indicated by the red dashed line, appears almost at the same location when comparing Fig. 5a and b, and when comparing Fig. 5c and d.

Figure 6 shows the relative error of the pressure field, computed as

$$e = \frac{|P_{\text{Hele-Shaw}} - P_{\text{Stokes}}|}{P_{\text{Stokes}}} \times 100\%. \quad (16)$$

We observe that the relative errors are within an acceptable range. The maximum error is around 13% but the majority of the error is below 5%.

3.2 Comparison against experiments

Recent experiments by Vani et al. [27] provide an invaluable opportunity for us to directly validate our modeling framework. These experiments feature mono-layered and mono-dispersed suspension flows through a constriction (Fig. 7). Since the system is quasi-bidimensional, we may reconstruct the simulation setup with the same channel geometry and particle properties (diameter, density, etc.) in 2D. In the experiments, the particle density and the fluid density are

the same, making the effect of gravity negligible. The ratio of constriction width to particle diameter, W/d , is kept as 1.7 to match the experimental setup. The particles are initiated at random positions.

We apply appropriate boundary conditions and solve the discrete system resulting from Eqs. (4) and (5). The left boundary is prescribed with a constant flow rate Q to mimic the experimental inflow conditions. Since the flow outlet is at ambient pressure, we prescribe a constant ambient pressure value at the constriction in the simulation. As in Sect. 3.1, the region outside the fluid-occupied domain is assigned with a negligibly small permeability to mimic no-flow boundary condition.

We consider a global damping constant ξ in the particle motion computations (see Supplementary Material). This feature helps to ensure numerical stability and to calibrate the particle flow, accounting for additional sources of dissipation not considered in the model. We then run batches of simulations of different particle packing ratios over a time period of 5 s. We verify that the rate of number of particles that escape from the constriction—we refer those particles as *escapees* (s) in the following paragraphs—approximates the reference experimental data as well as the empirical formula [27]

$$s(t) = \frac{4\phi Q}{H\pi d^2} t, \quad (17)$$

where ϕ is the surface packing fraction of particles in the control volume.

Since particle friction is unknown, assuming friction is directly related to clogging events, the model is calibrated to make sure the number of escapees before clogging approximates the reference experimental results. We tune the friction coefficient of the particles until the average escapees before clogging from 100 simulations agree with the experiments of the same packing fraction. A packing fraction of 0.26 was chosen as the benchmark case as it guarantees relatively quicker clogging events.

The fluid properties and particle properties [1] used in this section are shown in Tables 1 and 2.

Figure 8 shows the snapshots of a single simulation at different particle packing fractions (left) and averaged particle flow information across a period of 5 s (right). The particle information is recorded after achieving a steady stream of flow. Figure 8a,b show a reasonable agreement of escapee values with the empirical curve and the extracted experimental values for the lowest packing fraction (Fig. 8a). In the case of larger packing fractions (Fig. 8c), our solution overestimated the escapee number over time. This overestimation could be a result of the delicate difference between the 3D experimental setup and

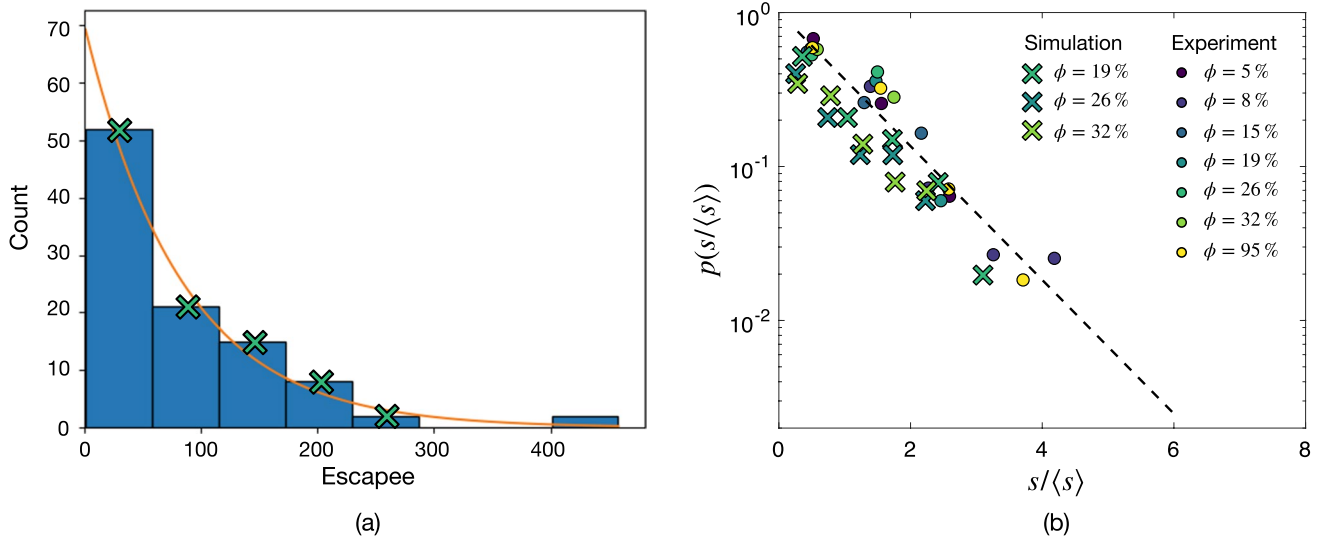


Fig. 9 **a** Histogram of the number of events N with different escapees s flowing through the constriction before clogging, with $W/d = 1.7$, $\phi = 0.26$ and $\mu = 0.25$. **b** Probability mass function (PMF) $p(s/\langle s \rangle)$

of the normalized escapees $s/\langle s \rangle$ before clogging, with experimental data shown in dots and simulation results shown in crosses (image adapted from [27])

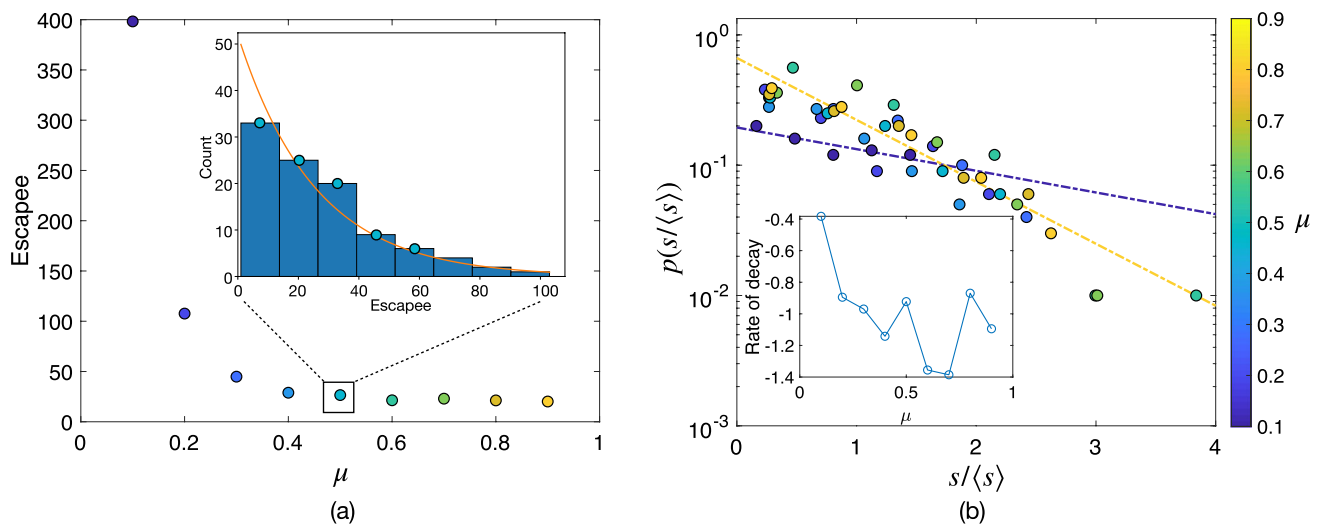


Fig. 10 **a** Average escapees s before clogging at $W/d = 1.7$ and $\phi = 0.26$ versus particle friction coefficient μ . Inset: Histogram of the number of events N with different escapees flowing through the constriction before clogging, with $\mu = 0.5$. **b** PMF $p(s/\langle s \rangle)$ of the normalized escapees $s/\langle s \rangle$ before clogging, with $0.1 \leq \mu \leq 0.9$. The two dashed lines show exponential data fitting with $\mu = 0.1$ (purple) and

$\mu = 0.9$ (yellow). From the two exponential fits, it is evident that the distribution of particles with a high friction coefficient decays faster than the distribution with a low friction coefficient. The rate of decay of the exponential fits for all friction coefficients is shown in the inset of (b) (color figure online)

our 2D simulation setup, or cumulative error from the simplified fluid-solid coupling.

We then perform 100 simulations, with all particles initialized at random positions, and record the number of escapees right before the flow path is completely clogged. We plot the histogram of the number of events N for which escapees s flow through the constriction before clogging happens. Figure 9a shows the geometric distribution of

simulations with $\phi = 0.26$ and $\mu = 0.25$. We see that it is more likely for clogging to happen after a small number of escapees, compared to the less likely cases where clogging occurs after more than 200 escapees. The probability of a clogging case with s escapees decreases exponentially as s increases.

Simulations with different packing fractions ($\phi = 0.19$ and $\phi = 0.32$) are further tested. We take the value of each

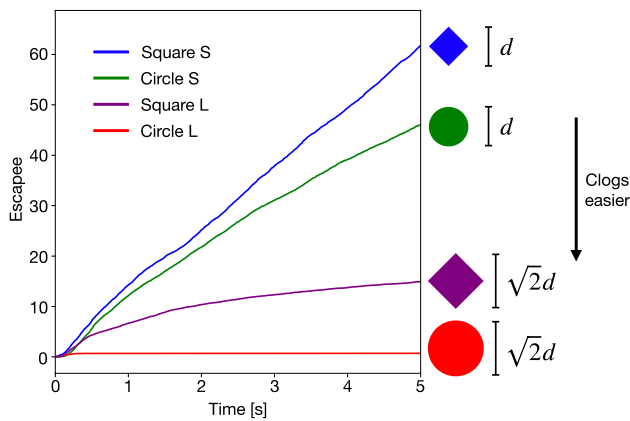


Fig. 11 Time evolution of escapees of different sized squares and circles

bin from histograms produced from the simulation results of all three packing fractions and plot the probability in log scale (Fig. 9b). We observe a negative linear trend between $p(s/\langle s \rangle)$ and $s/\langle s \rangle$, further indicating that the data collected from the simulations are exponentially distributed. Furthermore, we observe a good agreement between the simulated clogging statistics and the experimental results of Vani et al. [27].

In summary, in this section, we have shown that the pressure field calculated using the proposed Hele-Shaw flow model is relatively accurate in the particle-dense regions. Furthermore, we show good agreement between the extracted clogging statistics from simulations and experimental results.

With the proposed framework for simulating particle-laden incompressible flow, one can effectively model the flow of mono-layered particles of any shape through constrictions of any shape or size and with arbitrary flow boundary conditions in a relatively short computation time. For fluids with a low Reynolds number, the assumption of incompressibility keeps the formulation time-independent, allowing us to employ arbitrarily large increments when solving the fluid flow equations. Since the fluid force is calculated separately from the solid–solid interactions, the fluid pressure can be updated at a time spacing different from the time step of the solid particle motion. Moreover, in the traditional Stokes flow model, the solid boundary is generally remeshed after each fluid update. Conversely, the proposed model resolves the fluid pressure on a fixed mesh, which further cuts down computation time.

For simulations with a packing fraction $\phi = 0.17$ and a total of $2e7$ time steps (roughly 7.5 s in physical time), if we update the 159×135 fluid grid every $1e4$ time steps, the computation time is roughly 30 min for 2D spheres (using DEM) and 1 h for other shapes (using LS-DEM, each particle with 40 surface nodes). All simulations are executed with

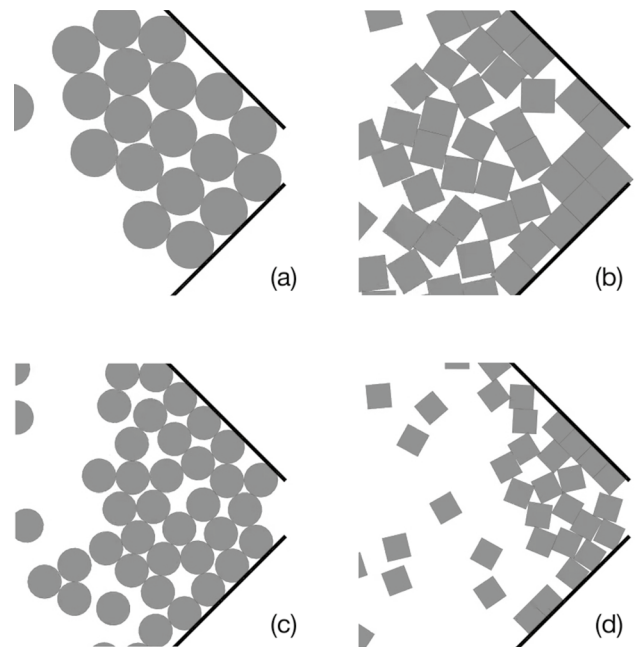


Fig. 12 Snapshots of clogged constriction with **a** circle L, **b** square L, **c** circle S, and **d** square S

a single thread. For larger packing fractions, parallelization using multiple threads can further increase the computation efficiency.

In the following section, we briefly discuss the effects of friction and particle shape on clogging using our proposed modeling framework.

4 Discussion

4.1 Effects of friction on clogging

We investigate the effect of particle friction on clogging statistics. Figure 10a shows the average number of escapees over 100 simulations versus the friction coefficient, with $\phi = 0.26$. We observe that the relationship between number of escapees and μ is hyperbolic. For $0.1 \leq \mu \leq 0.3$, averaged escapees drop quickly as the friction coefficient increases. At around $\mu = 0.5$, the rate of change flattens, indicating that given the current fluid environment, the static friction regime dominates for values above $\mu = 0.5$. Note that beyond $\mu = 0.5$, the average number of escapees fluctuates, possibly due to the sample size not being sufficiently large.

We again take the value of each bin from histograms produced from the simulation results of different friction coefficients (Fig. 10a inset) and plot the log-scaled PMF $p(s/\langle s \rangle)$ over normalized escapees (Fig. 10b). Intuitively, we

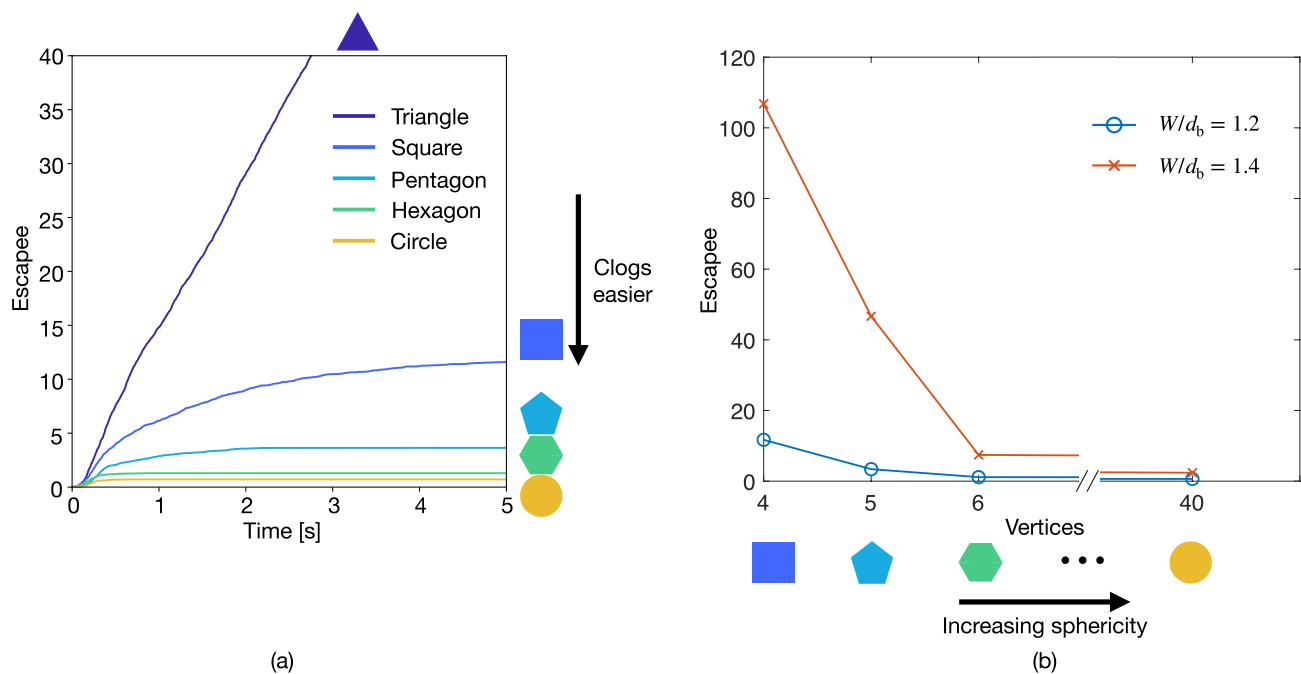


Fig. 13 **a** Time evolution of averaged escapees of particles with different shapes at the same bounding radius. **b** The average number of escapees before clogging versus the number of vertices at two W/d_b ratios

know that particles with different friction coefficients have different clogging probabilities. From the inset of Fig 10b, we see that the re-scaled PMFs collapse to exponential fits of different decay rates. As μ increases from 0.1 to 0.4, the rate of decay strictly increases in absolute value. This means that particles with larger friction coefficients tend to clog with fewer escapees, and the probability of clogging with more escapees decreases drastically as the friction coefficient increases. As μ increases from 0.5 to 0.9, the rate of decay does not show a clear relationship with increasing friction coefficient, possibly due to fluctuating mean values of escapees as seen in Fig. 10a where $\mu \geq 0.5$.

4.2 Effects of particle shape on clogging

All previous cases are simulated with circular-shaped particles. However, the proposed method is capable of simulating particles of arbitrary shapes. In order to investigate how particle shape affects clogging statistics, we compare simulations of square-shaped particles flowing through a narrow constriction with those of circular particles. Square-shaped particles have substantial significance in physical systems, as many crystals in nature are squares or rectangles in shape if observed in 2D. The precipitation, deposition, and/or accumulation of such solid particles like salt and mineral crystals during multi-phase flow through porous media is ubiquitous in many subsurface applications [18].

Since constriction width to particle-size ratio is also an important factor that could contribute to clogging [6], we simulate the time evolution of two different-sized square particles and compare them each to circular particles of the same bounding radius (Fig. 11). Due to shape differences, the same packing fraction no longer guarantees the same number of particles in the control volume. Therefore, a specific particle number is enforced in the control volume instead of the packing fraction. The ratio of the constriction width to the smaller and bigger bounding diameter is $W/d_b = 1.7$ and $W/d_b = 1.2$ respectively. To aid faster clogging, the friction coefficient is set to $\mu = 0.4$. All other solid and fluid parameters are kept the same as in Tables 1 and 2. For each particle shape, we perform 100 simulations to collect statistics.

In Fig. 11, we observe that clogging happens almost immediately for the larger circle (circle L). For the larger square (square L), clogging happens relatively slower. The slope flattens at around $t = 5$, indicating that the majority of the 100 simulations have clogged. The slopes for the smaller circle (circle S) and the smaller square (square S) decrease over time yet remain steep, as only a few simulations clog.

We group the four particle types into three pairs: the square S - circle S pair, for which the bounding radius is $d/2$ (d is the same as in Table 2); the circle S - square L pair, where the diameter of the circle equals the edge of the square; and the square L - circle L pair, for which the bounding radius is $d/\sqrt{2}$. We observe that for the square S - circle

S pair and the square L - circle L pair, circular particles clog with a smaller number of escapees. For the circle S - square L pair, square-shaped particles clog more easily.

We wish to unveil the reason behind this observation by looking at their clogged states (Fig. 12). To form a stable clog, particles need to first form a stable arch. For the square S - circle S pair (or the square L - circle L pair), the fact that the diagonal length of the square equals the diameter of the circle implies that squares need to have corner-corner type contacts whereas circles can have contacts anywhere along their circumference to form an arch of the same arc size. However, for the circle S - square L pair, since in this case the diagonal length of the square is $\sqrt{2}$ times the diameter of the circle, the presence of edges and corners promotes clogging through a higher number of contacts.

To further test the hypothesis that corners of polygons promote clogging, we release a group of regular polygons with different numbers of vertices – from equilateral triangles to regular hexagons—and simulate the time evolution of the averaged number of escapees through the constriction. We also simulate circles of the same bounding radius, as circles can have contacts everywhere along the bounding radius. To isolate the effect of particle size, we make sure all particles are bounded by the same radius. The constriction width to bounding diameter ratio is kept at 1.2. Again, due to shape differences, a specific number of particles in the control volume is enforced in the simulations instead of a packing fraction. From Fig. 13a, we observe that particles with more vertices tend to clog faster. All simulations with circles, hexagons, and pentagons are clogged by $t = 5$, as seen from the flattened curves. Simulations of squares and triangles have a higher number of escapees through the constriction by $t = 5$. Looking at the slope of the curves, the majority of the simulations with squares have clogged, while only a few simulations with triangles have clogged.

To better understand how clogging statistics are related to the number of vertices, we plot the averaged escapees before clogging versus the number of vertices present in the polygon (Fig. 13b). For the sake of simplicity, circles are modeled with 40 surface nodes, that is, with potential contacts on 40 vertices. In Fig. 13b, we see that as the number of vertices increases, the averaged escapees before clogging decrease drastically, almost in a hyperbolic trend. Circles have the least escapees before clogging since, with the same bounding radius, they are more likely to contact one another. Squares have the most escapees before clogging, as they only have four contacts along the bounding radius.

5 Conclusion

In this paper, we propose a simplified method to capture the dynamics of mono-layered particle-laden flow through a narrow constriction using LS-DEM coupled with Hele-Shaw type of flow. We first compare simulation results of circular-shaped particles before and at the clog with results produced by solving Stokes flow in COMSOL. We show satisfactory agreements between the pressure field around particle-occupied regions. We then show that after calibration, the particle statistics agree with experimental results from Vani et al. [27]. Lastly, we unveil a hyperbolic relationship between the averaged escapees before clogging and the friction coefficient of the particles, showing exponential fits of different rates of decay. We also show that particles with more vertices clog easier compared to particles with fewer vertices given the same bounding radius.

The use of Hele-Shaw flow model in replacement of the Navier–Stokes equation elegantly avoids the computational burden at a cost of accuracy; yet, we showed that the proposed method is still able to capture qualitatively the physics of clogging at the pore scale. The proposed method is not only capable of efficiently extracting particle statistics in quantity, but also providing meaningful and experimentally observed results. We show that one may not need to resolve the full detailed coupling between flow and particle mechanics to capture the statistical behavior of clogging in similar systems.

With the ability to study statistics of arbitrarily shaped particles through porous media, this method can be readily applied to investigate the influence of particle geometry, friction, constriction size, etc., on the clogging phenomenon. Furthermore, the use of the level set on the solid domain enhances flexibility in controlling particle shape morphing and provides opportunities for advanced shape control in a fluid environment, such as cases where the melting or freezing of the fluid affects the shapes of the solid particles.

The proposed method is readily expandable to 3D, capable of simulating particles of arbitrary shapes, and is easily coupled with particle bonding features [11] or fracture [10]. Such methods can efficiently simulate the three main mechanisms that contribute to clogging [6]—constriction size to particle size ratio, particle volume fraction, and surface cohesion. The former two can be easily modeled by modifying the pore geometry and particle statistics (shapes, size, volume fraction, etc.). The last contributing factor can be studied through the coupling of parallel or contact bonding.

Despite the merits of simplicity and straightforwardness, the proposed method unavoidably presents limitations. Since the current version only works in 2D and does not account for fluid shear force, it is best used for bidimensional systems with a small Reynolds number.

In conclusion, we propose a simple and direct method for mono-layered particle flow through simplified pore geometry. Simulation results produced by this method show qualitative agreements with experiments of identical setups. The proposed method can serve as a tool to enhance the understanding of particle-laden porous media flows, and to bridge the gap between particle properties and clogging mechanics.

Supplementary Information The online version contains supplementary material available at <https://doi.org/10.1007/s10035-024-01405-7>.

Funding JEA and ZZ would like to acknowledge the support from the National Science Foundation (NSF) under award number CMMI-2033779. JEA, RM and JU would like to acknowledge the support from the U.S. Army Research Office under grant number W911NF-19-1-0245. NJ and XF would like to acknowledge the support from the American Chemical Society (ACS) Petroleum Research Fund Doctoral New Investigator Grant under grant number 66867-DNI9.

Declarations

Conflict of interest The authors have no relevant financial or non-financial interests to disclose.

References

- Bizmark, Navid, Schneider, Joanna, Priestley, Rodney D., Datta, Sujit S.: Multiscale dynamics of colloidal deposition and erosion in porous media. *Sci. Adv.* **6**(46), eabc2530 (2020)
- Cundall, P.A.: Formulation of a three-dimensional distinct element model-Part I. A scheme to detect and represent contacts in a system composed of many polyhedral blocks. *Int. J. Rock Mech. Min. Sci. Geomech. Abstr.* **25**(3), 107–116 (1988)
- de Macedo, Robert, Buarque, Andò, Edward, Joy, Shilpa, Viggiani, Gioacchino, Pal, Kumar, Raj, Parker, Joseph, Andrade, José E.: Unearthing real-time 3d ant tunneling mechanics. *Proc. Natl. Acad. Sci.* **118**(36), e2102267118 (2021)
- Di Renzo, Alberto, Maio, Francesco Paolo Di.: Comparison of contact-force models for the simulation of collisions in dem-based granular flow codes. *Chem. Eng. Sci.* **59**(3), 525–541 (2004)
- Dincau, Brian, Dressaire, Emilie, Sauret, Alban: Clogging: the self-sabotage of suspensions. *Phys. Today* **76**(2), 24–30 (2023)
- Dincau, Brian, Tang, Connor, Dressaire, Emilie, Sauret, Alban: Clog mitigation in a microfluidic array via pulsatile flows. *Soft Matter* **18**, 1767–1778 (2022)
- Dressaire, Emilie, Sauret, Alban: Clogging of microfluidic systems. *Soft Matter* **13**, 37–48 (2017)
- Galindo-Torres, S.A.: A coupled discrete element lattice Boltzmann method for the simulation of fluid-solid interaction with particles of general shapes. *Comput. Methods Appl. Mech. Eng.* **265**, 107–119 (2013)
- Harmon, John M., Arthur, Daniel, Andrade, José E.: Level set splitting in DEM for modeling breakage mechanics. *Comput. Methods Appl. Mech. Eng.* **365**, 112961 (2020)
- Harmon, John M., Karapiperis, Konstantinos, Li, Liuchi, Moreland, Scott, Andrade, José E.: Modeling connected granular media: particle bonding within the level set discrete element method. *Comput. Methods Appl. Mech. Eng.* **373**, 113486 (2021)
- Johnson, K.L.: *Contact Mechanics*. Cambridge University Press, Cambridge (1985)
- Kawamoto, Reid, Andò, Edward, Viggiani, Gioacchino, Andrade, José E.: Level set discrete element method for three-dimensional computations with triaxial case study. *J. Mech. Phys. Solids* **91**, 1–13 (2016)
- Kloss, Christoph, Goniva, Christoph, Hager, Alice, Amberger, Stefan, Pirker, Stefan: Models, algorithms and validation for open-source DEM and CFD-DEM. *Progress Comput. Fluid Dyn. Int. J.* **12**(2–3), 140–152 (2012)
- Kuerten, J.G.M.: Point-particle DNS and LES of particle-laden turbulent flow—A state-of-the-art review. *Flow Turbul. Combust* **97**, 689–713 (2016)
- Lim, Keng-Wit., Andrade, José E.: Granular element method for three-dimensional discrete element calculations. *Int. J. Numer. Anal. Meth. Geomech.* **38**(2), 167–188 (2014)
- Material properties of Polystyrene and Poly(methyl methacrylate) (PMMA) microspheres. Technical report, Bangs Laboratories, Inc., 2015
- Mindlin, R.D., Deresiewicz, H.: Elastic spheres in contact under varying oblique forces. *J. Appl. Mech.* **20**(3), 327–344 (2021)
- Miri, Rohaldin, Hellevang, Helge: Salt precipitation during CO2 storage—a review. *Int. J. Greenhouse Gas Control* **51**, 136–147 (2016)
- Moncada, Rigoberto, Gupta, Mukund, Thompson, Andrew, Andrade, Jose E.: Level set discrete element method for modeling sea ice floes. *Comput. Methods Appl. Mech. Eng.* **406**, 115891 (2023)
- Qiang, Yuhao, Sissoko, Abdoulaye, Liu, Zixiang L., Dong, Ting, Zheng, Fuyin, Kong, Fang, Higgins, John M., Karniadakis, George E., Buffet, Pierre A., Suresh, Subra, Dao, Ming: Microfluidic study of retention and elimination of abnormal red blood cells by human spleen with implications for sickle cell disease. *Proc. Natl. Acad. Sci.* **120**(6), e2217607120 (2023)
- Ramkrishna, Doraiswami, Mahoney, Alan W.: Population balance modeling. Promise for the future. *Chem. Eng. Sci.* **57**(4), 595–606 (2002)
- Sahimi, M., Imdakm, A.O.: Hydrodynamics of particulate motion in porous media: Hydrodynamics of particulate motion in porous media. *Phys. Rev. Lett.* **66**, 1169–1172 (1991)
- Song, C.B., Park, H.S., Lee, K.W.: Experimental study of filter clogging with monodisperse PSL particles. *Powder Technol.* **163**(3), 152–159 (2006)
- Sun, B.H.: Hertz elastic dynamics of two colliding elastic spheres. *Results Phys.* **30**, 104870 (2021)
- Tsuji, Y., Kawaguchi, T., Tanaka, T.: Discrete particle simulation of two-dimensional fluidized bed. *Powder Technol.* **77**(1), 79–87 (1993)
- Vani, Nathan, Escudier, Sacha, Sauret, Alban: Influence of the solid fraction on the clogging by bridging of suspensions in constricted channels. *Soft Matter* **18**, 6987–6997 (2022)
- Wang, Yifan, Li, Liuchi, Hofmann, Douglas, Andrade, José, Daraio, Chiara: Structured fabrics with tunable mechanical properties. *Nature* **596**, 238–243 (2021)
- Wyss, Hans M., Blair, Daniel L., Morris, Jeffrey F., Stone, Howard A., Weitz, David A.: Mechanism for clogging of microchannels. *Phys. Rev. E* **74**, 061402 (2006)
- Xu, B.H., Yu, A.B.: Numerical simulation of the gas-solid flow in a fluidized bed by combining discrete particle method with computational fluid dynamics. *Chem. Eng. Sci.* **52**(16), 2785–2809 (1997)
- Xuxin, Tu., Andrade, José E.: Criteria for static equilibrium in particulate mechanics computations. *Int. J. Numer. Meth. Eng.* **75**(13), 1581–1606 (2008)
- Zhang, Fengshou, Wang, Tuo, Liu, Fang, Peng, Ming, Furtney, Jason, Zhang, Limin: Modeling of fluid-particle interaction by coupling the discrete element method with a dynamic fluid mesh:

- implications to suffusion in gap-graded soils. *Comput. Geotech.* **124**, 103617 (2020)
32. Zhou, Ziran, Andreini, Marco, Sironi, Luca, Lestuzzi, Pierino, Andò, Edward, Dubois, Frédéric., Bolognini, Davide, Dacarro, Filippo, Andrade, José E.: Discrete structural systems modeling: benchmarking of LS-DEM and LMGC90 with seismic experiments. *J. Eng. Mech.* **149**(12), 04023097 (2023)

Springer Nature or its licensor (e.g. a society or other partner) holds exclusive rights to this article under a publishing agreement with the author(s) or other rightsholder(s); author self-archiving of the accepted manuscript version of this article is solely governed by the terms of such publishing agreement and applicable law.

Publisher's Note Springer Nature remains neutral with regard to jurisdictional claims in published maps and institutional affiliations.